

Compression, spectral broadening, and collimation in multiple, femtosecond pulse filamentation in atmosphere

J. P. Palastro, T. M. Antonsen Jr., and H. M. Milchberg

Institute for Research in Electronics and Applied Physics, University of Maryland, College Park, Maryland 20740, USA

(Received 11 August 2012; published 24 September 2012)

A sequence of femtosecond laser pulses propagating through atmosphere and delayed near the rotational recurrence period of N_2 can resonantly drive molecular alignment. Through the polarization density, the molecular alignment provides an index of refraction contribution that acts as a lens copropagating with each laser pulse. Each pulse enhances this contribution to the index, modifying the propagation of subsequent pulses. Here we present propagation simulations of femtosecond pulse sequences in which we have implemented a self-consistent calculation of the rotational polarization density using linearized density matrix theory. We find that a femtosecond pulse sequence can enhance pulse compression or collimation in atmosphere. In particular, when the pulses are delayed by exactly the rotational recurrence period, each subsequent pulse is increasingly compressed due to a combination of spectral broadening and negative dispersion. Alternatively, when the intensity peak of each pulse is centered on the maximum index generated by the preceding pulses, each pulse is increasingly collimated.

DOI: [10.1103/PhysRevA.86.033834](https://doi.org/10.1103/PhysRevA.86.033834)

PACS number(s): 42.65.Re, 52.38.Hb, 92.60.Ta, 52.50.Jm

I. INTRODUCTION

During filamentary propagation in atmosphere, high power femtosecond laser pulses maintain high-energy fluence over extended distances due to a dynamic balancing of self-focusing and plasma refraction [1–3]. The potential for application coupled with basic physics interest in nonlinear, multiscale atomic and plasma phenomena has resulted in many investigations into filamentation of femtosecond pulses [4–13]. The key phenomenon associated with the extended propagation is the nonlinear polarization of the atmospheric constituents in the presence of the laser pulse. For propagation of infrared laser pulses the nonlinear polarization density includes several physical phenomena: the instantaneous electronic response, the delayed rotational response, the plasma response including ionization, and ionization energy damping.

The delayed rotational response of diatomic molecules found in atmosphere, namely N_2 and O_2 , exhibits “quantum recurrences” due to the regular spectrum of the rotational Hamiltonian [14–19]. This is manifested in recurrences in the index of refraction with a period of about 8.4 and 11.6 ps for N_2 and O_2 , respectively, following excitation by a short laser pulse. As a result, a second properly timed laser pulse will experience an index of refraction composed of not only its own enhancement to the molecular alignment but also that of the previous pulse. The recurrence contribution to the index has been shown to steer, focus, compress, shape, or even enhance THz generation of a second pulse [12,20–28]. With the exception of Zhdanovich *et al.* [26], who considered chiral alignment of O_2 in conditions far from atmospheric, all of these studies have considered only two pulses.

Here we present simulations of a sequence of six high power femtosecond laser pulses propagating through atmosphere delayed near the full recurrence period of N_2 . Each pulse in the sequence alters the molecular alignment and affects the propagation of all subsequent pulses. Prior two-pulse simulations [20,21,23,27] involve at least one of the following simplifications: single atmospheric molecular specie, weak pump or weak probe, one-dimensional propagation, or pure multiphoton ionization. The two-dimensional simulations pre-

sented here include the individual responses of both N_2 and O_2 , treat all pulses as nonweak, and include the Popruzhenko *et al.* (PMPB) ionization model [30], which is valid for intensities spanning the multiphoton to tunneling regime. In addition, we have implemented a self-consistent rotational response model valid for an arbitrary number of pulses based on the solution to the linearized (in intensity) rotational density matrix equation. At a point along the propagation path, the linearized density matrix (LDM) equation is solved numerically for every transverse position. The resulting nonlinear index of refraction then modifies the propagation to the next point along the path where the density matrix is resolved with the new intensity. The process then repeats. The density matrix solution ensures that the rotational polarization density is accurately modeled regardless of pulse delay or length.

This paper is organized as follows. Section II details our propagation model and atmospheric response models used in our simulations. In this section we describe our LDM model for the rotational polarization density and how we generalize the model for an arbitrary number of laser pulses. Intensity limitations of our LDM model are also discussed. In Sec. IV we present simulations of femtosecond pulse sequences propagating through atmosphere. Two cases are considered. In the first case each pulse is delayed by exactly the rotational recurrence period of N_2 , while in the second case each pulse is delayed to the peak of the rotational index generated by previous pulses. Section V concludes the paper with a summary of our results.

II. PROPAGATION AND ATMOSPHERIC RESPONSE MODEL

We begin by writing the electric field and nonlinear polarization density as an envelope modulated by a carrier wave at frequency ω_0 and axial wave number k :

$$E = \hat{E}(r, z, t)e^{i(kz - \omega_0 t)}, \quad (1a)$$

$$P_{NL} = \hat{P}_{NL}(r, z, t)e^{i(kz - \omega_0 t)}. \quad (1b)$$

Setting $k = k_0[1 + \delta\varepsilon(\omega_0)/2]$ where $k_0 = \omega_0/c$ and $\delta\varepsilon(\omega)$ is the shift in dielectric constant due to linear dispersion in atmosphere, and transforming to the moving frame coordinate $\xi = v_g t - z$ where $v_g = c[1 - \delta\varepsilon(\omega_0)/2]$ is the group velocity at frequency ω_0 , Eqs. (1a) and (1b) become

$$E = \hat{E}(r, \xi, z)e^{-ik\xi}, \quad (2a)$$

$$P_{\text{NL}} = \hat{P}_{\text{NL}}(r, \xi, z)e^{-ik\xi}. \quad (2b)$$

The evolution of the transverse component of the electric-field envelope is determined by the modified paraxial equation

$$\begin{aligned} & \left[\nabla_{\perp}^2 + 2 \frac{\partial}{\partial z} \left(ik - \frac{\partial}{\partial \xi} \right) - \beta_2 \frac{\partial^2}{\partial \xi^2} \right] \hat{E}_{\perp} \\ & = 4\pi \left(ik - \frac{\partial}{\partial \xi} \right)^2 \hat{P}_{\text{NL}, \perp}, \end{aligned} \quad (3)$$

where $\beta_2 = \omega_0 c (\partial^2 k / \partial \omega^2)|_{\omega=\omega_0}$ accounts for group velocity dispersion. In our simulations we use the experimentally determined value of β_2 in air, $\beta_2 = 20 \text{ fs}^2/\text{m}$ [31,32]. We note that in deriving Eq. (3), v_g/c has been approximated by unity when it appears as a coefficient. Furthermore we have assumed that the filament electron densities will be small enough such that $\nabla \cdot E \simeq 0$. From here on, the subscript \perp while not written is implied.

The nonlinear polarization density can be expressed as the sum of a free-electron contribution, \hat{P}_f , and a molecular contribution, \hat{P}_m :

$$\hat{P}_{\text{NL}} = \hat{P}_f + \hat{P}_m. \quad (4)$$

The free-electron polarization density includes the plasma response as well as a term accounting for the pulse energy lost during ionization. In particular the evolution of \hat{P}_f can be written in the convenient form

$$\begin{aligned} & \left(ik - \frac{\partial}{\partial \xi} \right)^2 \hat{P}_f \\ & = \frac{1}{4\pi} \left[\frac{\omega_p^2}{c^2} - i \frac{8\pi}{\omega_0} \left(\frac{U_N v_N \eta_N + U_O v_O \eta_O}{|\hat{E}|^2} \right) \right] \hat{E}, \end{aligned} \quad (5)$$

where U_a , η_a , and v_a are the ionization potential, molecular number density, and ionization rate for specie a , respectively, $\omega_p^2 = 4\pi e^2 \eta_e / m_e$, η_e is the electron number density, e is the fundamental unit of charge, m_e is the electron mass, and the subscripts N and O refer to molecular nitrogen and oxygen. The electron density and molecular densities evolve according to

$$\frac{d\eta_e}{d\xi} = v_N \eta_N + v_O \eta_O, \quad (6a)$$

$$\frac{d\eta_a}{d\xi} = -v_a \eta_a, \quad (6b)$$

respectively. The ionization rates are calculated via the PMPB model [30]. In calculating v_a , the values of U_a and post-ionization atomic charge Z_a are adjusted from their atomic values to match the experimental results of Talebpour *et al.* for molecular ionization [33]. For nitrogen we use $U_N = 15.6 \text{ eV}$ and $Z = 0.9$, while for oxygen $U_O = 12.1 \text{ eV}$ and $Z = 0.53$ [33]. We note that ionization of O_2 provides the dominant contribution to the plasma density.

The molecular contribution to the polarization density is the product of the total nonlinear molecular susceptibility and the electric field:

$$\hat{P}_m = (\chi_{\text{elec}} + \chi_{\text{rot}}) \hat{E}, \quad (7)$$

where χ_{elec} is the instantaneous electron susceptibility and χ_{rot} the delayed rotational susceptibility. The electronic susceptibility is given by

$$\chi_{\text{elec}} = \frac{1}{16\pi^2} \left(\frac{\eta_N n_{2,N} + \eta_O n_{2,O}}{\eta_{\text{atm}}} \right) c |\hat{E}|^2, \quad (8)$$

where $\eta_{\text{atm}} = 2.6 \times 10^{19} \text{ cm}^{-3}$, $\eta_N = 0.8\eta_{\text{atm}}$, and $\eta_O = 0.2\eta_{\text{atm}}$ upstream from the laser pulse, and the $n_{2,a}$ are the experimental values obtained by Wahlstrand *et al.*, namely, $n_{2,N} = 7.4 \times 10^{-20} \text{ cm}^2/\text{W}$ and $n_{2,O} = 9.5 \times 10^{-20} \text{ cm}^2/\text{W}$ [34]. Recent experiments have verified that the nonlinear electronic response depends quadratically on the laser field amplitude all the way to the ionization threshold [35]. The contribution of argon, which comprises only 1% of atmosphere by volume, has been neglected in Eq. (8).

We now present a model for rotational susceptibility based on LDM theory that can be generalized to an arbitrary number of pulses. Typically a simple harmonic-oscillator (SHO) model is used for the rotational susceptibility in one-pulse simulations [2]. In our previous work, we proposed and implemented an extension of the SHO model for rotational recurrences [28,29], which is a fit to the LDM model implemented here. The LDM response model results in extended simulation times, but prevents the accumulation of error due to repeated use of a fit in pulse stacking simulations. While the LDM formalism has been considered in simulations devoted solely to the molecular response, it has not, to our knowledge, been previously implemented self-consistently into laser-pulse propagation simulations.

The rotational susceptibility in atmosphere is

$$\chi_{\text{rot}} = \eta_N \Delta\alpha_N [\langle \cos^2 \theta \rangle_N - \frac{1}{3}] + \eta_O \Delta\alpha_O [\langle \cos^2 \theta \rangle_O - \frac{1}{3}], \quad (9)$$

where $\Delta\alpha_a = \alpha_{\parallel,a} - \alpha_{\perp,a}$; $\alpha_{\parallel,a}$ and $\alpha_{\perp,a}$ are the linear polarizabilities along and perpendicular to the molecular bond axis, respectively; θ is the angle between the molecular axis and the laser electric field; and the brackets, $\langle \rangle$, represent an ensemble average. As with the values of $n_{2,a}$, the values of $\Delta\alpha_a$ are those measured in the experiments of Wahlstrand *et al.*: $\Delta\alpha_N = 7 \times 10^{-25} \text{ cm}^3$ and $\Delta\alpha_O = 1.1 \times 10^{-24} \text{ cm}^3$ [34].

Determination of $\langle \cos^2 \theta \rangle$ quantum mechanically requires solving for the evolution of the density matrix, ρ . We write the total wave function as a superposition of spatial functions forming a complete set, $u_n(\vec{r})$, with time dependent amplitudes, $c_n(t)$: $\psi(\vec{r}, t) = \sum_n c_n(t) u_n(\vec{r})$. An element of the density matrix, ρ_{mn} , is defined as the ensemble average of $c_m^*(t) c_n(t)$. The matrix evolves according to

$$\frac{\partial \rho}{\partial t} = \frac{i}{\hbar} [\rho, H], \quad (10)$$

where H is the Hamiltonian and $[\]$ denotes the commutator. The diagonal elements of the density matrix represent the probability that a molecule is in a particular rotational state while the off diagonal elements represent interference

between states. A spatially dependent applied potential couples elements of the density matrix, causing transitions between states and resulting in a transfer of probability from one state to another. The expectation value of $\cos^2 \theta$ is given by $\langle \cos^2 \theta \rangle = \text{Tr}[\rho \cos^2 \theta]$, where Tr denotes the trace operation.

In the rigid rotor model of a linear diatomic molecule experiencing a torque in the presence of a laser electric field, it is useful to expand ψ in the basis of angular momentum eigenstates. We write H as the sum of two terms, $H = H^0 + V(t)$. The first term, $H^0 = (p_\theta^2 + \sin^{-2} \theta p_\phi^2)/2I_M$, is the Hamiltonian for a field free rigid rotor with eigenvalues $E_j = \hbar^2 j(j+1)/2I_M$ where j is the orbital quantum number and I_M is the moment of inertia. The second term, $V(t) = (\alpha_\perp + \Delta\alpha \cos^2 \theta)|\hat{E}|^2/4$, is the potential associated with the torque imparted by the laser-pulse electric field. In particular,

$$H = \frac{p_\theta^2}{2I_M} + \frac{1}{\sin^2 \theta} \frac{p_\phi^2}{2I_M} - \frac{1}{4}[\alpha_\perp + \Delta\alpha \cos^2 \theta]|\hat{E}|^2. \quad (11)$$

We expand the density matrix as $\rho = \rho^0 + \rho^1 + \dots$ where the superscripts on ρ denote perturbation order. The results of the expansion to first order are equations for ρ^0 and ρ^1 , namely,

$$\frac{\partial \rho_{ab}^0}{\partial t} = -i\omega_{ab}\rho_{ab}^0, \quad (12a)$$

$$\frac{\partial \rho_{ab}^1}{\partial t} = -i\omega_{ab}\rho_{ab}^1 + \frac{i}{\hbar}[\rho^0, V]_{ab}, \quad (12b)$$

where $\omega_{ab} = (E_a - E_b)/\hbar$, the subscripts refer to (j, m) pairs, $\rho_{ab} = \rho_{jm, j'm'}$, and m is the quantum number associated with the z component of the angular momentum. For a laser pulse with FWHM σ satisfying $\sigma\omega_{ab} \ll 1$, one can show that an approximate condition for convergence of the perturbation series is $\sigma\Delta\alpha|\hat{E}|^2/16\hbar < 1$. In the simulations presented below, the maximum intensity or clamping intensity, where ionization induced refraction limits self-focusing, is $\sim 3 \times 10^{13}$ W/cm². Using this intensity and a FWHM of 50 fs, we find $\sigma\Delta\alpha_N|\hat{E}|^2/16\hbar = 0.7$. While this seems marginal, previous experiments and nonlinear calculations demonstrate that linear theory reasonably represents regions of transient alignment up to $\sigma\Delta\alpha_N|\hat{E}|^2/16\hbar \sim 1$ [17–19]. In particular for $\sigma\Delta\alpha_N|\hat{E}|^2/16\hbar = 0.7$, we find the difference in the linear alignment and nonlinear alignment to be a constant positive offset of 5% of the maximum alignment [18,19].

Assuming the gas starts in thermodynamic equilibrium, the zeroth-order density matrix is

$$\rho_{ab}^0 = \delta_{ab} Z_p^{-1} D_j \exp\left[-\frac{\hbar^2 j(j+1)}{2I_M T}\right], \quad (13)$$

where T is the temperature, D_j is a degeneracy factor associated with nuclear spin, and Z_p is the partition function

$$Z_p = \sum_{j=0} (2j+1) D_j \exp\left[-\frac{\hbar^2 j(j+1)}{2I_M T}\right]. \quad (14)$$

For the simulations presented in the next section, we use a typical atmospheric temperature of $T = 294$ K.

Upon working through the algebra, we find

$$\langle \cos^2 \theta \rangle - \frac{1}{3} = \frac{\Delta\alpha}{\hbar} \frac{2}{15} \sum_j \frac{j(j-1)}{2j-1} \left(\frac{\rho_{jj}^0}{2j+1} - \frac{\rho_{j-2, j-2}^0}{2j-3} \right) \times \int_{-\infty}^{\xi} \sin\left[\frac{\omega_{j, j-2}}{c}(\xi' - \xi)\right] |\hat{E}|^2 d\xi', \quad (15)$$

where $\rho_{jj}^0 = \sum_m \langle m | \rho_{ab}^0 | m \rangle$. Equation (15) is a summation over solutions to independent, driven harmonic-oscillator equations. The total rotational susceptibility can then be written as a sum of contributions from each rotational quantum state $\chi_{\text{rot}}(\xi) = \sum_j \chi_j(\xi)$, where each χ_j satisfies a harmonic-oscillator equation with a driving term proportional to the intensity of the laser pulse:

$$\begin{aligned} & \left[\frac{d^2}{d\xi^2} + \omega_{j, j-2}^2 \right] \chi_j \\ &= -\frac{2\rho(\Delta\alpha)^2}{15\hbar} \frac{j(j-1)}{2j-1} \left(\frac{\rho_{jj}^0}{2j+1} - \frac{\rho_{j-2, j-2}^0}{2j-3} \right) \omega_{j, j-2} |\hat{E}|^2. \end{aligned} \quad (16)$$

To determine the number of total angular momentum states required for finding χ_{rot} , we define the thermal, total angular momentum through the relationship $j_{th}(j_{th} + 1) = 2I_M T/\hbar^2$. For N₂ and O₂ at 294 K, we find $j_{th} \simeq 10 \simeq 12$ respectively. In our simulations we solve Eq. (16) for 25 j states at every position along the propagation path and at every radial position for both N₂ and O₂.

The LDM model for the susceptibility can be generalized to an arbitrary number of laser pulses. After the first laser pulse has passed, the solution of Eq. (16) can be found after a time interval Δt through the relationship

$$\chi_j(\xi) = \cos[\omega_{j, j-2} \Delta t] \chi_j(\tau) + \frac{\sin[\omega_{j, j-2} \Delta t]}{\omega_{j, j-2}} \frac{\partial \chi_j(\tau)}{\partial \tau}, \quad (17)$$

where $\tau = \xi/c - \Delta t$ is anytime after the first pulse but before the second pulse. Thus given the solution at τ , the solution at the same point in space after an interval Δt is given by Eq. (17). The total rotational susceptibility experienced by the second pulse is then $\chi_{\text{rot}, 2}(\xi) = \sum_j \chi_{j, 2}(\xi) + \sum_j \chi_{j, 1}(\xi)$, where the second subscript denotes the pulse ordering and $\chi_{j, 2}(\xi)$ is the solution to Eq. (17) driven by the second pulse. In general, the n th pulse experiences a rotational susceptibility of

$$\chi_{\text{rot}, j}(\xi) = \sum_{i=1}^n \sum_j \chi_{j, i}(\xi). \quad (18)$$

Thus, in order to find the susceptibility experienced by the n th laser pulse we record the intensity profile of the subsequent pulses and numerically solve Eqs. (16) and (17).

III. SIMULATION RESULTS

We simulate the evolution of a sequence of six laser pulses by solving Eq. (3) in azimuthally symmetric cylindrical coordinates, with the susceptibilities defined in Sec. II. The propagation of the laser pulses is simulated over a distance of 5.5 m starting from a focusing lens with a 3-m focal length and $f_\# = 590$. The initial transverse profile of each pulse

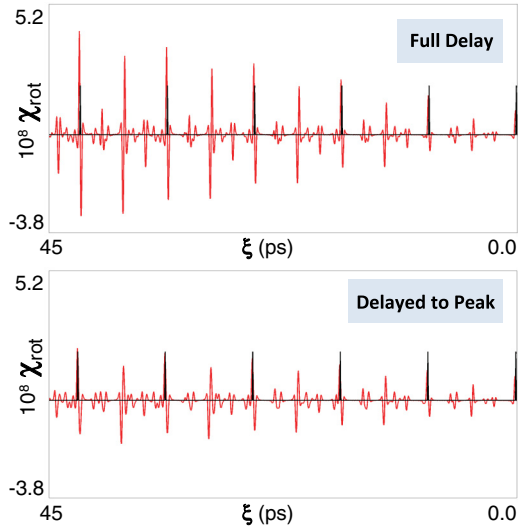


FIG. 1. (Color online) On-axis rotational susceptibility immediately after the lens as a function of time for two different sets of delays. The pulses in the sequence, with temporal FWHM plotted to scale, are discernible as the black lines. In the top plot each pulse is delayed by exactly the N_2 recurrence period, while in the bottom plot each pulse is delayed to the peak in susceptibility generated by the previous pulses.

is Gaussian with an initial spot radius (e^{-1} of the field) of 0.26 cm and a vacuum focal spot radius of 300 μm . The initial longitudinal intensity profile is $\sin^4(\pi\xi/\sigma)$ for $0 < \xi < \sigma$, with $\sigma = 139$ fs. The corresponding FWHM is $\sigma_{\text{FWHM}} \simeq 0.36\sigma$ or 50 fs. To evaluate the rotational susceptibility generated by previous pulses, we record the intensity profile of each pulse in both the r and ξ coordinates every 1.16 cm along the entire propagation path. The recorded intensity is then interpolated to the position of the current pulse for evaluating Eqs. (16) and (17). The resulting susceptibility is then used in Eq. (3) for evolving the current pulse.

We consider two cases: one in which each laser pulse is delayed by a full recurrence period of N_2 and the other in which each laser pulse is delayed to the maximum rotational index generated by the previous pulses right after the focusing lens. Figure 1 depicts the on-axis susceptibility resulting from density matrix theory as a function of ξ at a longitudinal position immediately after the lens for a sequence of six 2-mJ pulses. The positions of the laser pulses with accurate widths are plotted in black for reference. For the full recurrence delay the pulses resonantly drive the molecules into alignment with each subsequent pulse providing additional alignment. For the peak delay the pulses do not drive the molecules in phase, resulting in less overall alignment. As we will see, both situations result in significantly different laser-pulse evolution. We note that a region of negative susceptibility precedes the full recurrence while a region of positive susceptibility follows the recurrence. Figure 2 plots the delays used in the simulation relative to the full nitrogen recurrence periods.

A. Full N_2 recurrence delay

We first consider the propagation characteristics of pulses delayed by a full N_2 recurrence period. Each pulse sits at

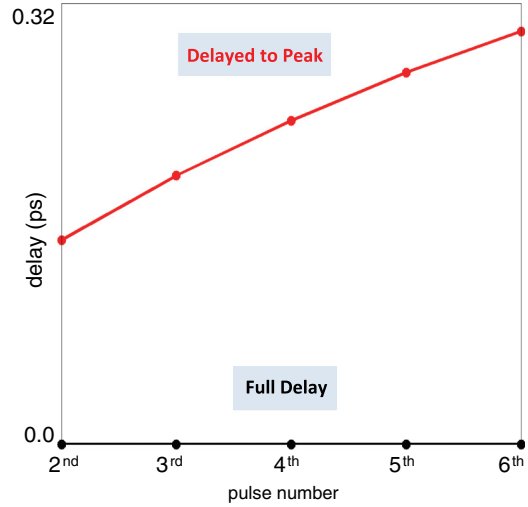


FIG. 2. (Color online) Delays used in our simulations with respect to a full N_2 recurrence period.

exactly the zero crossing of the rotational alignment generated by the preceding pulses. Thus the front of the pulse will experience a negative index and the back of the pulse a positive index. Figure 3 shows the accumulated on-axis electron density generated after the first and sixth pulses as a function of propagation distance. In Fig. 3(a) each pulse has 2 mJ of energy. Only the first pulse contributes significantly to the electron density. The refraction of each pulse from the electron density can be observed in the fluence shown in Fig. 4 for the 2-mJ pulse sequence. For clarity, the fluence is normalized by the maximum at each longitudinal position. The first pulse self-focuses, collimates, and ultimately diffracts. The subsequent pulses self-focus, refract from the plasma generated predominately by the first pulse, refocus, and finally refract. During both refraction stages, the later pulses refract more strongly than the earlier pulses but experience similar electron-density profiles.

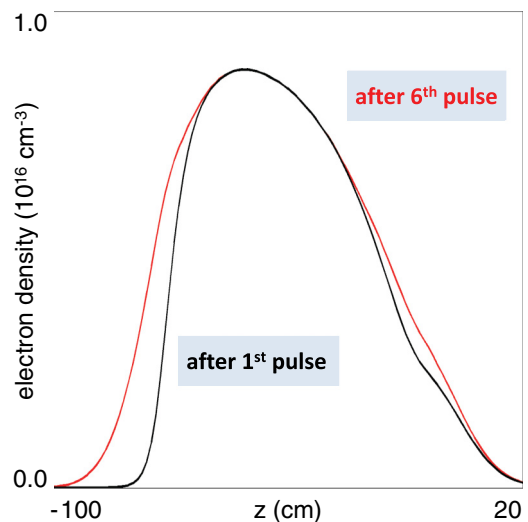


FIG. 3. (Color online) Accumulated on-axis electron density as a function of distance from focus following the first and sixth pulses.

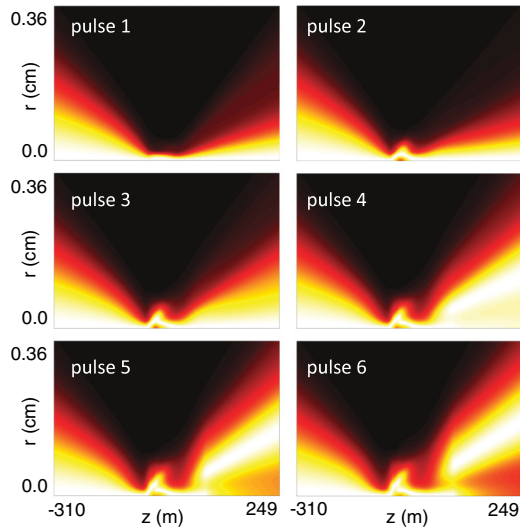


FIG. 4. (Color online) Energy fluence as a function of radius and distance from focus for each pulse. For clarity the fluence has been normalized by the maximum at each longitudinal position.

To explain the additional refraction we consider the motion of the longitudinal centroid of the laser pulse defined as follows:

$$\langle \xi(z) \rangle = \frac{\int \xi |E|^2 d\xi d^2r}{\int |E|^2 d\xi d^2r}. \quad (19)$$

Figure 5(a) depicts $\langle \xi \rangle$ for the second and sixth pulses as a function of propagation distance. The centroid of both pulses initially slides backwards due to the nonlinear group velocity being less than the linear group velocity. The group velocity of both pulses then increases and the centroids move forward. The increase in group velocity results from a combination of spectral red-shifting and negative dispersion. As the pulses

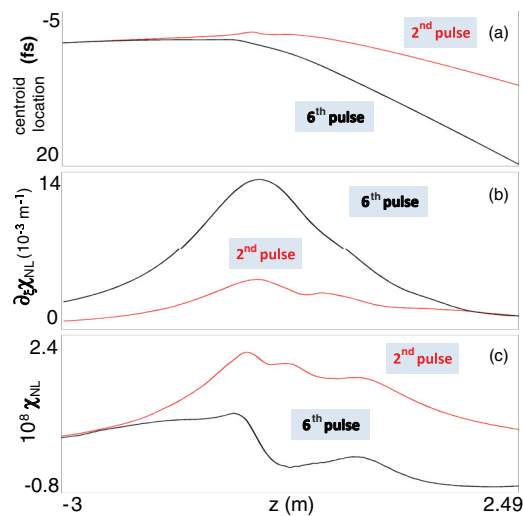


FIG. 5. (Color online) (a) Temporal location of the centroid in the moving frame relative to its initial location for the second and sixth pulses. (b) Differential susceptibility experienced by the centroid of the second and sixth pulses. (c) Nonlinear susceptibility including the plasma contribution experienced by the centroid of the second and sixth pulses.

focus, their intensity increases, enhancing the molecular alignment. In addition to their self-generated alignment, the later pulses will experience the enhanced molecular alignment from earlier pulses. The enhanced molecular alignment leads to a larger index of refraction causing spectral red-shifting through the relationship

$$\frac{\partial}{\partial z} \left(\frac{\delta\lambda}{\lambda_0} \right) \simeq 2\pi \frac{\partial \chi}{\partial \xi}. \quad (20)$$

Figure 5(b) shows the radially averaged gradient of the total susceptibility, including the plasma contribution, experienced by the centroid as a function of propagation distance. At the peak of the susceptibility gradient the pulses are strongly red-shifted, increasing their group velocity. The enhanced susceptibility from the previous pulses results in the sixth pulse having a larger group velocity than the second. As the pulses speed up, they move forward with respect to the alignment recurrence into the region of negative index. This lower index causes the pulses to refract as seen in Fig. 4. The later pulses refract more strongly for two reasons: their higher group velocity moves them further into the negative index region, and the index in this region is more negative from the contribution of the preceding pulses. Figure 5(c) shows the total radially averaged susceptibility experienced by the centroids. As expected the sixth pulse experiences a lower nonlinear index than the second pulse and thus refracts more strongly.

While the enhanced red-shifting and negative dispersion cause the later pulses to refract more strongly, they also result in significant longitudinal compression. In Fig. 6, the radially averaged intensity profiles normalized by the maximum after 5.5 m of propagation are plotted. The initial FWHM is plotted for reference. Each pulse is longitudinally compressed to a greater extent than the pulse before it. As discussed in the above paragraph the centroid of each subsequent pulse is further ahead in the moving frame. The bottom plot shows the full

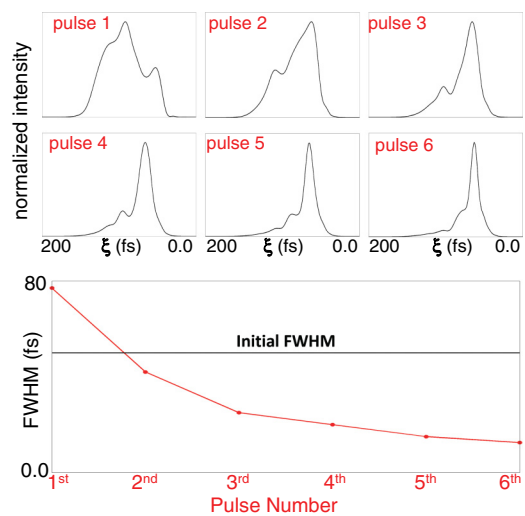


FIG. 6. (Color online) On top the radially averaged longitudinal profiles of each pulse plotted as a function of moving frame coordinate after 5.5 m of propagation. On bottom the FWHM as a function of pulse number is displayed. A line for the initial FWHM is included for reference.

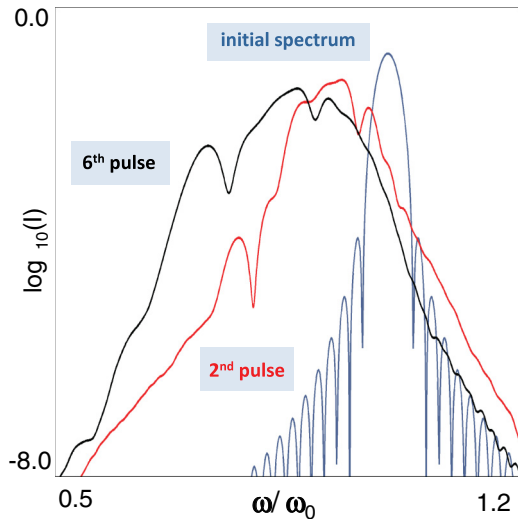


FIG. 7. (Color online) The radially averaged spectrum of the second and sixth pulses after 5.5 m of propagation. The initial spectrum for both pulses is plotted for reference.

width half maximum (FWHM) of each pulse. In our previous work with slightly lower energy and longer pulses, Ref. [29], a second pulse delayed by exactly the recurrence period was not observably compressed or spectrally broadened; it only appeared shortened due to spatial filtering. Pulse compression results from negative dispersion and a positive index gradient in the pulse frame due to the index recurrence. If the molecular alignment is weak, the gradient is small, and red-shifting and hence compression are minimal. In Ref. [29], the index gradient experienced by the second pulse was not large enough to result in compression. Similarly, for our current parameters the second pulse is not significantly compressed as seen in Fig. 6. Because each additional pulse enhances the alignment, each subsequent pulse experiences a larger index gradient, and is increasingly compressed. As to be expected, the longitudinal compression is accompanied by spectral broadening. Figure 7 displays the laser-pulse spectrum averaged over radius after 5.5 m of propagation for the second and sixth pulses. The initial spectrum of both pulses is also plotted for reference. In addition to the red-shift of the spectral peak, the bandwidth of the second and sixth pulses has increased by a factor of 3 and 4.8, respectively.

B. Peak delay

We now consider the evolution of pulses delayed to the peak of the rotational alignment generated by the previous pulses. Each pulse initially experiences a positive index throughout its duration and copropagates with the molecular alignment recurrence. Figure 2 plots the actual delays relative to the full recurrence time. The pulses are delayed by more than 100 fs from the full recurrence period of 8.38 ps. Figure 8 displays the accumulated on-axis electron-density profile after each pulse. As opposed to delaying to the full recurrence, each pulse contributes significantly to the electron density.

For a single pulse, refraction results from the plasma and molecular nonlinearities differing in their transverse extent. The molecular nonlinearities have the same transverse profile

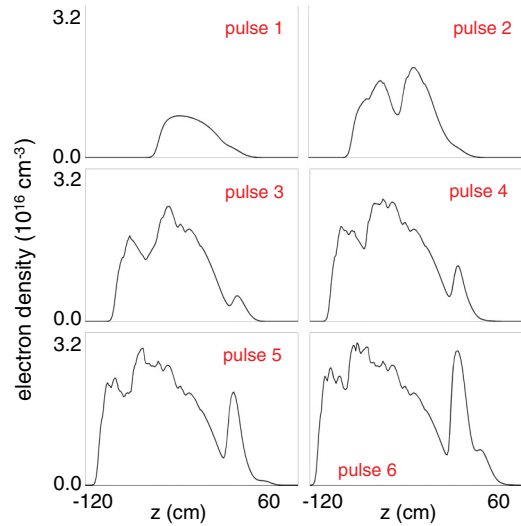


FIG. 8. (Color online) Accumulated electron density as a function of distance from vacuum focus for each pulse.

as the pulse intensity with a width of approximately the spot size. In the multiphoton ionization regime for O_2 , the plasma nonlinearity has a transverse width of approximately one fourth the spot size (the ionization rate is $\propto |\hat{E}|^{16}$). As the pulse focuses and ionizes, the plasma contributes a negative index localized at the center of the pulse. The transverse index profile has minimum on axis, increases out to some radius, then decreases to zero. The positive transverse gradient in index results in refraction.

With multiple pulses delayed to the peak of the rotational alignment, the recurrence contribution reduces the transverse index gradient experienced by the second to sixth pulses. As a result, these pulses focus strongly enough to further ionize the air as opposed to refracting from the plasma generated by earlier pulses. When the later pulses ionize, a newly formed transverse index gradient develops due to the additional plasma. The pulses then refract, their intensity

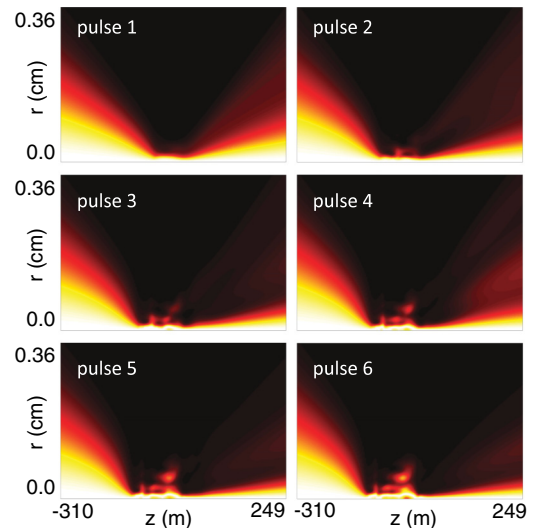


FIG. 9. (Color online) Energy fluence as a function of radius and distance from focus for each pulse. For clarity the fluence has been normalized by the maximum at each longitudinal position.

drops, and ionization terminates. As discussed below, this process can repeat for each pulse. After ionization terminates the positive recurrence contribution that has accumulated with each additional pulse reduces diffraction. The positive index of the rotational recurrence acts as a travelling lens that helps collimate each pulse.

The increased collimation is observed in Fig. 9, which shows the fluence of each pulse normalized by the maximum at each longitudinal position. Several cycles of focusing and refraction can be discerned in Fig. 9 with each focusing point corresponding to a peak in the density shown in Fig. 8. After ionization the positive index limits diffraction and the pulses maintain a narrow spot. From Fig. 8 we see that the additional plasma generated by the n th pulse is less than that generated by the $(n - 1)$ th pulse. As a result, in addition to being a narrower spot, the later pulses contain more energy after 5.5 m of propagation: The second and sixth pulses have 1.1 and 1.4 mJ, respectively.

IV. SUMMARY AND CONCLUSIONS

We have investigated the atmospheric propagation of a sequence of six femtosecond laser pulses delayed near the rotational recurrence period of N_2 . To model the recurrences in the molecular alignment, we have implemented a self-consistent density matrix model for the rotational contribution to the polarization density. Each pulse in the sequence experiences its own enhancement to the molecular alignment as well as the contribution from all preceding pulses. In addition to the molecular polarization density, the nonlinear index of refraction includes contributions from the instantaneous electronic response, the plasma response where the nonlinearity shows up through the intensity dependence of the ionization rate, and ionization energy damping. All parameters in the

nonlinear polarization are based on up-to-date experimental measurements.

Propagation simulations were conducted for two sets of delays: pulses delayed by exactly one N_2 recurrence period and pulses delayed to the peak in molecular alignment generated by the preceding pulses. In the first situation, only the first pulse contributed significantly to the plasma density. Although the pulses encountered a similar plasma density profile during propagation, each subsequent pulse refracted more strongly. As the pulses copropagated with the susceptibility gradient from the molecular alignment, they red-shifted, increasing the group velocity. The increase in group velocity resulted in the pulses moving forward into the negative index region of the molecular recurrence, causing additional refraction. This same process resulted in each subsequent pulse being increasingly compressed: the bandwidth of the sixth pulse had increased by nearly a factor of 5 over 5.5 m of propagation.

When the pulses were delayed to the peak of the rotational index, ionization by each pulse contributed to the electron density. The increase in plasma, however, did not result in an increase in refraction. On the contrary, each pulse was increasingly collimated. The rotational index, which was greater for each subsequent pulse, acted as a travelling lens, keeping the pulses focused. In addition to a tighter focus, the n th pulse contained more energy than the $(n - 1)$ th after 5.5 m of propagation. These simulations demonstrate that properly timing the delays in femtosecond pulse sequences can provide compression and spectral broadening or increased collimation.

ACKNOWLEDGMENTS

The authors would like to thank P. Sprangle, J. K. Wahlstrand, W. Zhu, L. Johnson, T. Rensink, and C. Miao for fruitful discussions. The authors would also like to thank ONR, NSF, and the Department of Energy for support.

-
- [1] A. Braun *et al.*, *Opt. Lett.* **20**, 73 (1995).
 - [2] A. Couairon and A. Mysyrowicz, *Phys. Rep.* **441**, 47 (2007).
 - [3] P. Sprangle *et al.*, *Phys. Rev. E* **66**, 046418 (2002).
 - [4] M. Mlejnek *et al.*, *Phys. Rev. Lett.* **83**, 2938 (1999).
 - [5] A. Couairon and L. Berge, *Phys. Plasmas* **7**, 193 (2000).
 - [6] J. R. Penano *et al.*, *Phys. Rev. E* **68**, 056502 (2003).
 - [7] G. Méchain *et al.*, *Appl. Phys. B* **79**, 379 (2004).
 - [8] G. Méchain *et al.*, *Phys. Rev. Lett.* **93**, 035003 (2004).
 - [9] A. Ting *et al.*, *Appl. Opt.* **44**, 1474 (2005).
 - [10] M. Nurhuda and E. van Groesen, *Phys. Rev. E* **71**, 066502 (2005).
 - [11] S. Eisenmann *et al.*, *Phys. Rev. Lett.* **100**, 155003 (2008).
 - [12] S. Varma *et al.*, *Phys. Rev. Lett.* **101**, 205001 (2008).
 - [13] Y.-H. Chen *et al.*, *Phys. Rev. Lett.* **105**, 215005 (2010).
 - [14] C. H. Lin *et al.*, *Phys. Rev. A* **13**, 813 (1976).
 - [15] H. Stapelfeldt and T. Seideman, *Rev. Mod. Phys.* **75**, 543 (2003).
 - [16] E. Hamilton *et al.*, *Phys. Rev. A* **72**, 043402 (2005).
 - [17] Y.-H. Chen *et al.*, *Opt. Express* **15**, 11341 (2007).
 - [18] A. J. Pearson and T. M. Antonsen, *Phys. Rev. A* **80**, 053411 (2009).
 - [19] J. P. Palastro *et al.*, *Phys. Rev. A* **84**, 013829 (2011).
 - [20] R. A. Bartels *et al.*, *Phys. Rev. Lett.* **88**, 013903 (2002).
 - [21] V. Kalosha *et al.*, *Phys. Rev. Lett.* **88**, 103901 (2002).
 - [22] A. York and H. M. Milchberg, *Opt. Express* **16**, 10557 (2008).
 - [23] J. Wu *et al.*, *Opt. Lett.* **33**, 2593 (2008).
 - [24] H. Cai *et al.*, *Opt. Express* **17**, 21060 (2009).
 - [25] M. Durand *et al.*, *Opt. Lett.* **35**, 1710 (2010).
 - [26] S. Zhdanovich *et al.*, *Phys. Rev. Lett.* **107**, 243004 (2011).
 - [27] F. Calegari *et al.*, *Phys. Rev. A* **79**, 023827 (2009).
 - [28] S. Varma *et al.*, *Phys. Rev. A* **86**, 023850 (2012).
 - [29] J. P. Palastro *et al.*, *Phys. Rev. A* **85**, 043843 (2012).
 - [30] S. V. Popruzhenko *et al.*, *Phys. Rev. Lett.* **101**, 193003 (2008).
 - [31] E. R. Peck and K. Reeder, *J. Opt. Soc. Am.* **62**, 958 (1972).
 - [32] P. Wrzesinski *et al.*, *Opt. Express* **19**, 5163 (2011).
 - [33] A. Talebpour *et al.*, *Opt. Commun.* **163**, 29 (1999).
 - [34] J. K. Wahlstrand *et al.*, *Phys. Rev. A* **85**, 043820 (2012).
 - [35] J. K. Wahlstrand *et al.*, *Phys. Rev. Lett.* **109**, 113904 (2012).